Experimental and Numerical Investigations of SBLI and Flow Control on a Transonic Compressor Cascade

Edwin J. Munoz Lopez and Alexander Hergt

Abstract The flow through a transonic compressor cascade is inherently unsteady due to the shock-boundary layer interactions (SBLI) on the blade. Despite decades of research, few details are known about the mechanisms that cause such behavior. This chapter presents a multidisciplinary study aiming to elucidate these mechanisms and optimize flow control methods to mitigate their effects. For this purpose, the Transonic Cascade TEAMAero was first optimized and its performance was validated experimentally. The cycle of shock oscillation was then compared using advanced experimental measurement techniques and high-fidelity LES. This comparison revealed a continuous propagation of pressure waves from a point upstream of the trailing edge. The interaction of these waves with the main bow shock at different points of the cycle was then linked to the frequencies observed in the oscillation spectrum. A configuration of this cascade with two roughness patches was finally optimized using a novel procedure developed. The optimal configurations obtained show how the targeted design of these devices can simultaneously mitigate shock oscillations and improve performance. This chapter demonstrates how the combined application of advanced numerical and experimental techniques needs to be intensified as researchers search for a global theory of SBLI in compressor blades.

Keywords Transonic flow · Shock induced separation · Advanced experimental methods · Flow control optimization

E. J. Munoz Lopez (✉) · A. Hergt
German Aerospace Center (DLR), Cologne, Germany
e-mail: edwin.munozlopez@dlr.de

A. Hergt
e-mail: alexander.hergt@dlr.de

P. Flaszynski et al. (eds.), *Towards Effective Flow Control and Mitigation of Shock Effects in Aeronautical Applications*, Notes on Numerical Fluid Mechanics and Multidisciplinary Design 201, https://doi.org/10.1007/978-3-031-86605-0_14

1 Introduction

Unsteady shock-boundary layer interactions (SBLI) are ubiquitous to sonic flows. The inevitable presence of these two complex features allows many hypotheses why their interaction is highly unsteady. These interactions were first observed from as early as the 1940s [1, 2], though the measurement techniques at the time did not allow for detailed analyses on the sources of unsteadiness. Only in recent decades and with the help of advanced numerical and experimental methods, comprehensive hypotheses have been formulated and tested to explain this phenomenon [3, 4]. These hypotheses typically involve mechanisms of propagation of disturbances in the downstream direction from the incoming flow, or in the upstream direction from the turbulent flow downstream of the shock, or in both directions from the interaction of the shock with its own separation bubble [5–9].

Within the context of compressor blades, the unsteady SBLIs are known to reduce the performance and robustness of typical designs, among other issues [10, 11]. In recent decades, the prevalent theory of shock oscillation for applications of aerodynamic profiles seems to be Lee's trailing edge feedback mechanism [5, 12, 13]. According to Lee, the vortical structures created at the shock foot interact with the trailing edge to create pressure waves that influence the position of the shock continuously. Previous numerical studies of different fidelity levels have found evidence to this theory on different compressor blade designs [14, 15]. However, experimental studies in the past have also shown evidence of disturbances originating and propagating from a region downstream of the shock, but upstream of the trailing edge [16]. Due to the complexity posed by such configurations, further research is required to achieve a more complete understanding of all the mechanisms at play.

A high level of interest is also present in the study and application of flow control methods (FCM) to mitigate these oscillations. Early studies of these devices were focused on vortex generators (VG) with configurations of co-rotating or counter-rotating vortices [17, 18]. More recently, shapes have emerged that are specifically conceptualized to mitigate unsteady SBLI effects, such as the shock control bump (SCB) [19, 20]. In principle, these shapes aim to fix the shock in place and also generate vortices to aid flow reattachment. Regardless of the FCM to be studied, it is clear that their design requires a robust optimization procedure. This is necessary to methodically explore the design space for a set of optimal designs that could mitigate shock oscillations and improve the performance of the given design.

The Institute of Propulsion at the DLR has fortunately accumulated an extensive amount of experience in the fields pertaining to the study of SBLIs and FCMs on compressor cascades. This is observed in the experimental studies with advanced measurement techniques in Hergt et al. [11, 22], Klinner et al. [16, 21], but also in the numerical studies with advanced numerical methods for blade design in Voß et al. [23], Aulich et al. [24], Schnoes et al. [25] and for high-fidelity simulations in Klose et al. [26], Morsbach et al. [27], Bergmann et al. [28]. This expertise was fully leveraged within the context of the doctoral work performed for the TEAMAero research consortium. The content of this work is only briefly summarized in this chapter,

with readers being referred to a future publication of the whole monograph for further detail. This chapter then begins by presenting a brief overview of the baseline compressor cascade designed for the consortium, following a detailed analysis of the unsteady SBLIs on this cascade with advanced experimental and numerical techniques, and finally presenting the novel numerical optimization procedure developed to mitigate them.

2 The Transonic Cascade TEAMAero

The Transonic Cascade TEAMAero (TCTA) is a new compressor cascade optimized at the DLR with the typical design tools developed and available at the institute of propulsion. The main purpose of this new design was to serve as a baseline geometry for the different objectives previously outlined. This section then first provides a brief overview of the design process before presenting the experimental campaign carried out at the DLR's Transonic Cascade Wind Tunnel (TGK) to validate its performance.

2.1 Optimization Process Overview

For a detailed breakdown of the optimization performed, the reader is referred to Munoz Lopez et al. [29, 30]. The process chain built for this optimization consisted of three main procedures: generating a new cascade geometry, meshing the cascade, and estimating its performance through RANS simulations. The simulations were performed with the DLR's in-house CFD solver, TRACE, and applying the k-ω SST model coupled with the $\gamma - Re_{\Theta}$ transition model [31, 32]. The result from this process chain was managed by the DLR's optimization suite, AutoOpti, which was set to minimize two objectives: the flow losses at the aerodynamic design point (ADP), and over the working range (WR) at a constant inlet Mach number (M_1^{ADP}). The flow losses were quantified at each operating point by the total pressure loss coefficient (ω).

The ADP for the optimization was set to a Mach number of 1.20, an inflow angle of 145.8°, and an axial velocity density ratio (AVDR) of 1.20. The latter being a parameter that quantifies the amount of flow area contraction at the outlet compared to the inlet due to the growth of the sidewall's boundary layer (BL) [33]. This effect was simulated in the numerical domain with contracting inviscid sidewalls. The operating point was further constrained by the aerodynamic loading, as measured with the de Haller number (DH). After finding the ADP by adjusting the outlet pressure in the simulations, the WR was determined by methodically increasing and decreasing the inflow angle until the cascade stalled or choked, respectively.

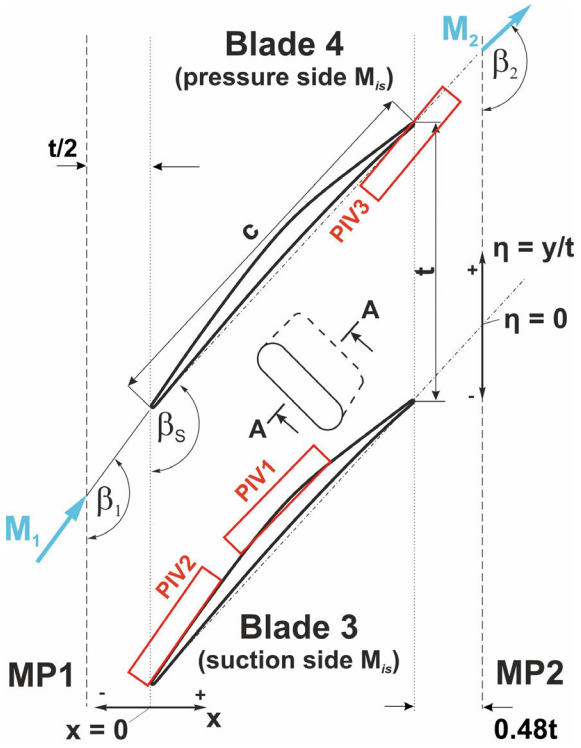

Fig. 1 Transonic cascade TEAMAero—design definition

The optimization results yielded several candidate designs from the Pareto front. A number of post-optimization analyses at different off-design points (ODP) were performed to pick the candidate with the most robust performance for the final TCTA design. This design is shown in Fig. 1, as manufactured for the experimental campaign. The cascade's main geometrical properties are summarized in Table 1, along with its validated performance for an AVDR of 1.05. These conditions were found to be the most stable for measurements in the wind tunnel, as discussed in the following sections. The performance properties also correspond to test number (TN) 125, as described in Munoz Lopez et al. [34].

2.2 Experimental Validation

This work package was finalized with an experimental campaign at the DLR's Transonic Cascade Wind Tunnel (TGK) in order to validate the performance of the TCTA cascade [34]. For this purpose, the final cascade design from Fig. 1 was manufactured with a total of six blades and installed in the TGK in Cologne. The experimental configuration of the cascade in the wind tunnel is shown in Fig. 2. This figure shows

Table 1 Transonic cascade TEAMAero—properties of interest

General properties	
Blade chord, c (mm)	100
Pitch, t (mm)	65
Stagger angle, β_{st} (°)	135.8
Blade span, s (mm)	168
Aerodynamic design point properties	
Inflow Mach, M_1	1.20
Reynolds number, Re (10^6)	1.35
Inflow angle, β_1 (°)	145.7
Axial velocity density ratio, AVDR	1.05
de Haller number, DH	0.582
Flow turning, FT (°)	10.1
Total pressure loss coefficient, ω	0.1132

the different features of the wind tunnel used to adjust the operating conditions in the test section, as well as the motorized wake probe assembly used to measure the conditions at the outlet.

The focus of this experimental campaign was to validate the steady performance of the cascade, as optimized in Sect. 2.1. In order to perform these measurements, a number of steady measurement techniques were employed at the inlet measurement plane (MP) 1, outlet MP2, and over the blade suction and pressure surfaces. These included pressure tap measurements at these locations of interest, but also three-hole probe measurements at the MP2, and Laser-2-Focus (L2F) measurements at the MP1. The latter is a type of laser anemometry technique developed at the DLR in

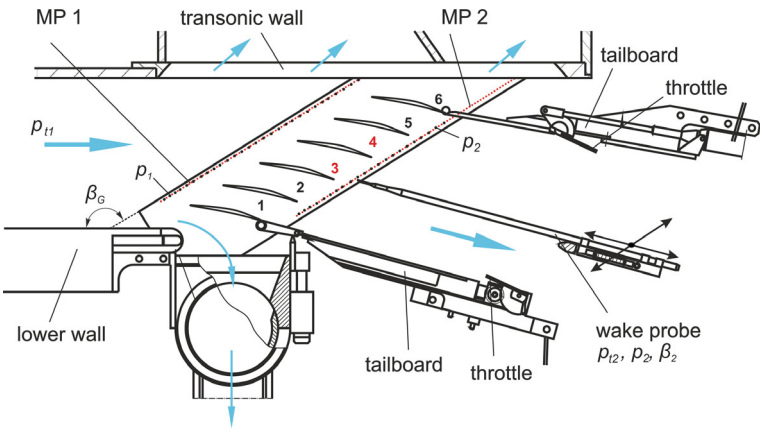

Fig. 2 Experimental configuration of the TCTA installed in the TGK

(a) TCTA cascade (b) TGK test section with the TCTA cascade installed

Fig. 3 TCTA assembly and wind tunnel configuration for the experiments

Schodl [35] that allows the measurement of the inflow angle without obstructing the supersonic flow. For more details on the application and challenges of using these techniques to measure this inherently unsteady SBLI flow, the reader is referred to the extensive discussion published in Munoz Lopez et al. [34]. The standalone cascade assembly and the fully instrumented configuration for the tests are shown in Fig. 3.

The main results validated the expected losses of the cascade within a margin of error of 3–6% throughout the working range at an AVDR of 1.05, as shown in Fig. 4a. In this figure, the measurement points are labeled with their test numbers (TN), where TN125 corresponds to the ADP of the cascade and TN78 indicates the onset of choke. The cascade also shows a high aerodynamic loading in Fig. 4b, with more than 10° flow turning at the ADP. This high loading is achieved over a wide working range of at least 2°. The TN27 taken from choked conditions at an AVDR of 1.00 is also shown. This measurement demonstrates the difficulty of capturing the correct onset of choke numerically, which depends strongly on the AVDR of the cascade. The reader is referred to Munoz Lopez et al. [34] for further comparisons of flow visualizations, the isentropic Mach number (M_{is}) distributions, the wake loss profiles, and others.

3 The Unsteady SBLI on the Transonic Cascade TEAMAero

The flow through a transonic compressor cascade is highly unsteady, and the TCTA is no exception. The study of these unsteady SBLIs is a difficult undertaking both experimentally and numerically due to the small temporal and spatial scales involved. This means that advanced configurations are required in order to observe, quantify, and simulate such interactions. In this section, a short overview of the detailed study of

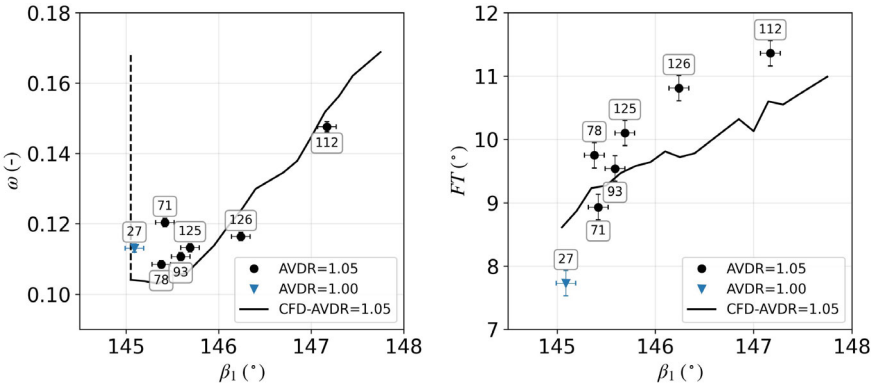

(a) Total pressure loss coefficient polar (b) Flow turning polar

Fig. 4 Working range performance of the TCTA: CFD and experimental results comparison

the unsteady SBLI on the TCTA will be presented [36]. This is Part 3 of a three-part publication detailing the oscillation of the shock via advanced experimental techniques in Part 1 [37] and advanced numerical methods in Part 2 [38]. In Part 3, the results from high-fidelity LES simulations, high-speed shadowgraph (HSS), and particle image velocimetry (HSPIV) measurements are analyzed together. This section briefly discusses the preliminary studies performed, before presenting the advanced numerical and experimental methods, followed by a description of the shock oscillation cycle, the validation of the LES results with the experimental measurements, and finally a summary of the mechanisms of unsteadiness identified.

The preliminary studies consisted of two experimental campaigns performed to quantify the interactions to be studied. The first one consisted of capturing standard 2D-2 component and high-resolution snapshot PIV images, as shown in Klinner et al. [39]. These images provided a detailed look at the averaged flow field through the cascade, revealing a mean shock position of 52.6% with respect to the blade's chord. proper orthogonal decomposition (POD) analyses also revealed some of the main spatial modes of oscillation of the shock, although these could not be linked to any frequencies yet. The flow through the cascade was then measured via HSS at 20 kHz, as described in Munoz Lopez et al. [40]. This was done over three adjacent cascade passages to study the joint movement of their shock structures. These studies revealed that the shock in the passage of the TCTA oscillates at a broad frequency band between 500 and 550 Hz, which is modulated by a high-frequency tone at 1140 Hz and its harmonics. The information gathered helped prepare the advanced experimental and numerical investigations presented in the following sections.

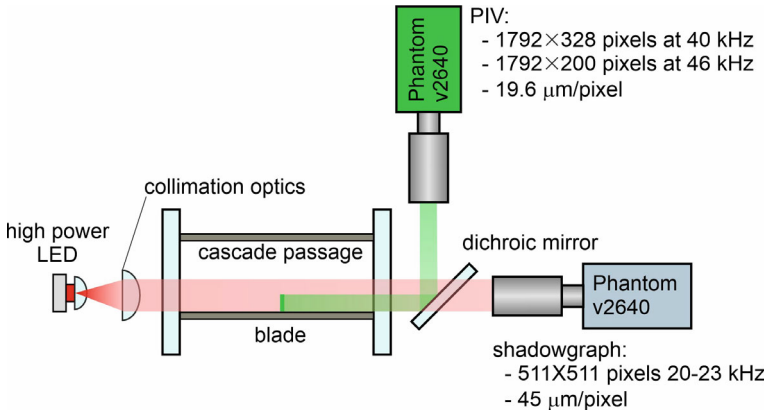

Fig. 5 Experimental configuration for simultaneous capturing of time-resolved shadowgraphy and PIV

3.1 Advanced Experimental and Numerical Methods for SBLI Flows

In order to gather the most amount of information possible on the unsteady SBLI over the TCTA, advanced numerical and experimental techniques were applied on the ADP of the cascade. By leaning on both set of results, the limitations of the experimental measurements could be overcome, and the high-fidelity simulations could be thoroughly validated. This section first provides a brief overview of the experimental configuration used to capture HSS and HSPIV images of the shock at the TCTA's ADP, before describing the numerical configuration for the main LES simulation performed on the ADP of the cascade.

3.1.1 Advanced Experimental Methods for SBLI Flows

The main objective was to obtain detailed footage in different regions of interest that could be compared directly to the LES simulations. This was done with HSPIV recordings at the regions marked in Fig. 1. These are relatively small due to the limitations of current hardware, allowing fields of view of $31 \times 6.4\,\text{mm}^2$ with a pixel density of 19.6 μm/pixel. In order to complement these recordings, simultaneous HSS recordings are performed with a bigger field of view of 33×33 mm^2 and a magnification of 45 μm/pixel on which the shock position can be tracked. Even though hardware issues did not allow the perfect synchronization of these recordings, the two sets of high-speed measurements allow for a unique insight into the flow in the passage. The configuration required for such measurements with two Phantom v2640 HS cameras capturing sampling rates of 20 or 23 kHz is shown in Fig. 5.

A typical measurement run with this setup would consist of 8 different bursts of up to 10 thousand shadowgraph images and 20 thousand PIV images per burst. The PIV images are evaluated in window sizes of either 64×32 or 64×16 pixels to obtain validation rates higher than 95% of the cross-correlated image pairs. The shadowgraph images on the other hand are typically processed directly from the tiff raw data files with different regions of interest depending on the desired evaluation. For instance, to apply either shock-tracking algorithms over the entire shock region, or smaller windows for the evaluation of PSD contours or wave propagation analyses. For more details on the configuration and the processing of the results, the reader is referred to the cited publications.

3.1.2 Advanced Numerical Methods for SBLI Flows

The simulation results used for this study were calculated with TRACE's discontinuous Galerkin spectral method (DGSEM) solver. The implementation and validation of this method for has been described in detail in Klose et al. [26], Morsbach et al. [27], Bergmann et al. [28]. For the numerical part of this work package, an extensive comparison was performed between URANS and LES simulations of different resolutions [38]. For the analyses presented in this section, only the results from the fully resolved LES mesh are used. Its main feature is the long simulation time computed, which was required to capture converged statistics on the main low frequency band of shock oscillations around 500 Hz.

In this simulation, the operating conditions are set to match those of the experiments from TN125, as presented in Sect. 2.2. The only deviation is the periodic boundary conditions in the spanwise direction, which sets an AVDR of 1.00 instead of 1.05. This implies a higher loading of the cascade and a more upstream mean position of the shock over the blade. Nevertheless, the conditions are similar enough to provide a good comparison with the experiments. The rest of the domain consists of an inlet 1.0 chord length upstream of the leading edge, and an outlet 1.5 chord lengths downstream of the trailing edge of the blade. These boundaries apply 1D non-reflecting boundary conditions via the method of flow characteristics in Schlüß et al. [41]. The operating conditions are set by specifying the total pressure, total temperature, and inflow angle at the inlet, as well as the static pressure at the outlet.

The mesh used for the simulation is generated as a 2D slice with the Gmsh package and contains 108,564 rectangular elements with structured refinements around the shock locations. The mesh is then extruded by 10% of the chord length in the spanwise direction, with elements set to a polynomial order of 3 to provide a 4th order accurate spatial discretization. The simulation is advanced in time explicitly via a 3rd order Runge-Kutta scheme. The maximum non-dimensional cell sizes in the mesh are within recommended levels in the streamwise, wall-normal, and spanwise directions: $\Delta\xi^+_{\max} = 35$, $\Delta\eta^+_{\max} = 2$, and $\Delta\zeta^+_{\max} = 25$. These values are normalized by the polynomial order given to compare with finite volume simulations. Finally, the domain is sampled with 1D probe lines and a coarser 2D regular grid for analysis. A

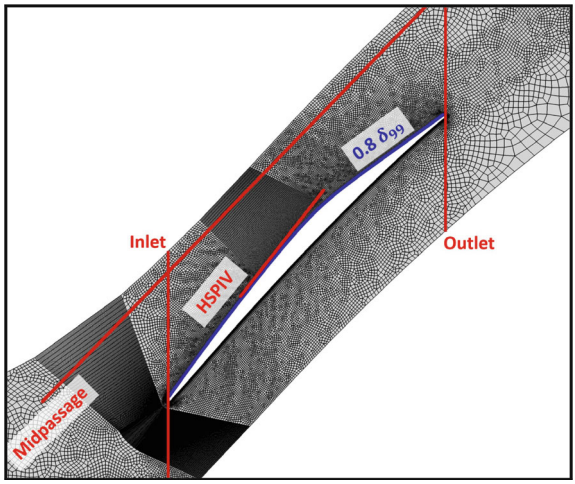

Fig. 6 Coarse TCTA mesh for simulations with TRACE's DGSEM LES solver

coarse version of the domain and some of the most relevant probe lines sampled are shown in Fig. 6.

3.2 The Cycle of Shock Oscillation

The experimental results amount to more than 56 s of footage from the 14 measurement runs with 8 bursts each. The LES results on the other hand correspond to more than 100 convective time units (CTU) of simulation time, but still amount to 'only' 30 ms of footage. The results must then be analyzed with care in order to draw meaningful conclusions from them. The first evaluation is performed by tracking the shock position over time for both datasets. For the HSS results, this is done via an image gradient sensor over pixel rows of the images. Outliers are searched along the pixel rows and then again along image sequences to obtain the most accurate measurement of the shock position. For the LES results, the shock can be tracked with high precision along the midpassage probe line shown in Fig. 6 by applying a modified ducros sensor as in Pirozzoli et al. [42].

The resulting signals can then be evaluated with power spectral densities (PSD) by applying the Welch method, as shown in Fig. 7. The figure shows that the oscillation of the shock is much more tonal in the LES than the experiments. The peak of the main oscillation is also strongly marked in the LES at 614 Hz, while the experiments show a broad peak around 513 Hz. Even if these peaks differ by about 100 Hz, they still lie remarkably close to each other with respect to any other such comparison found in the literature. This figure also shows a second PSD for the LES results obtained from an imperfect shock tracking from a probe line closer to the blade surface and applying a density gradient sensor. These results more closely resemble those of the

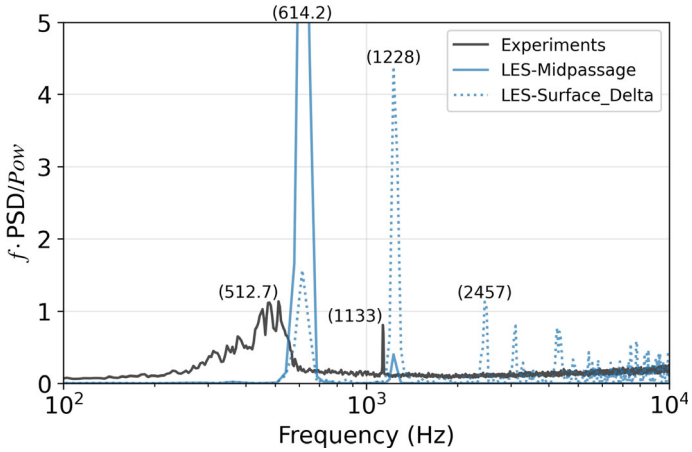

Fig. 7 Power spectral densities of the shock position in the experiments and the LES results

experiments, with stronger high-frequency tones and a broader low-frequency peak of oscillation.

This simple comparison informs the rest of the results in this section, whereby the authors demonstrate that these two datasets show the same mechanisms of shock oscillation and not necessarily that they are replicas of each other. This would be impossible due to the different factors affecting the flow in the experiments: the lack of perfect periodicity, the sidewall suction in the passage, the limited stiffness of the blade, and others. For a more comprehensive description, the readers are referred to the discussions in Munoz Lopez et al. [34, 36].

The shock oscillation in the passage of the TCTA is now described by leaning on the detail offered by the LES results. This is done in Fig. 8 with roughly equi-temporal Mach contours of one entire cycle of shock oscillation. In these snapshots, some of the main features of the mechanisms to be investigated can already be observed. The shock starts at its most upstream position, and a weak oblique shock is observed to be propagating upstream in the sonic region of the flow over the blade. An acoustic wave just upstream of the trailing edge has also formed from the apparent interaction of the separated flow convecting downstream from the previous cycle. These waves take the form of shocklets that start interacting with the main shock as it moves into the passage. The strong interaction between these features seems to produce a momentary choking that culminates in a strong oblique shock propagating upstream. The resulting breakdown of the flow under the shock foot produces a column of separated flow that convects downstream to complete the cycle.

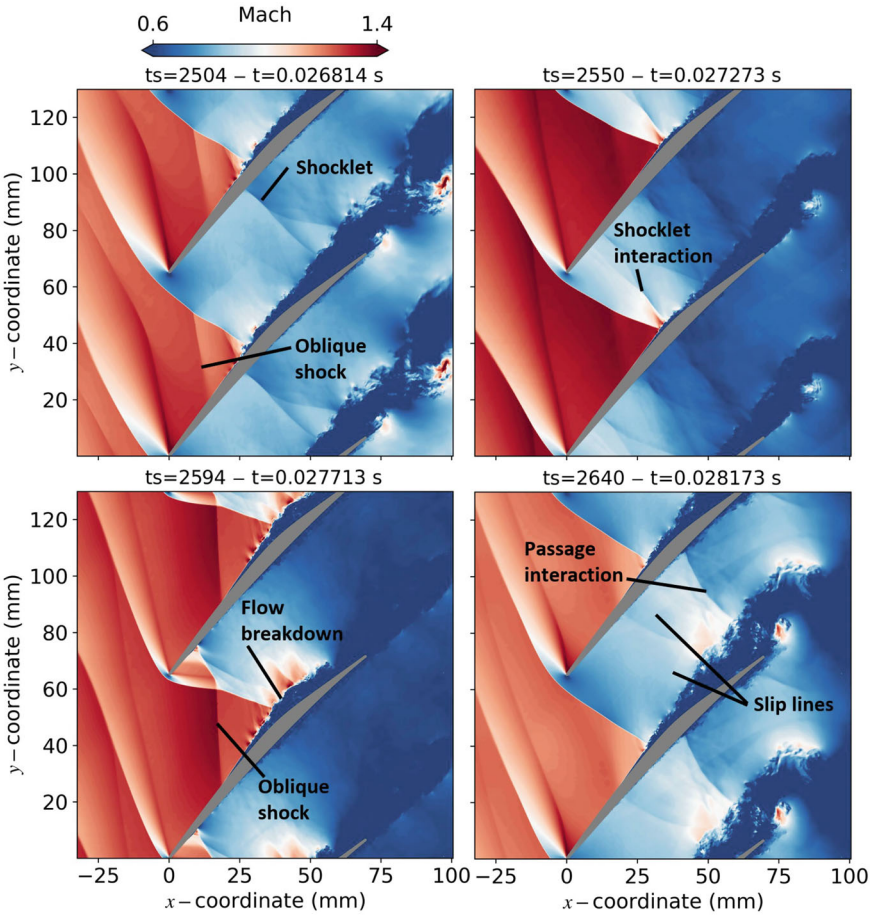

Fig. 8 Mach contours of one shock oscillation cycle over the TCTA

3.3 Validating LES Simulations with Experimental Measurements

The cycle of oscillation from the LES results observed in the previous section is now validated by comparing it directly with the experimental results via qualitative and quantitative methods. For this purpose, Fig. 9 shows a cycle of shock oscillation as observed from two similar cross-correlated sequences of HSS and HSPIV images. In this sequence, the same shocklet features previously noted can be observed to propagate upstream in the subsonic region of the flow. The movement of the shock into the passage also coincides with the interaction of the shocklets and the increase of the flow separation under the shock foot. This interaction is also observed to generate weak and strong oblique shocks that propagate upstream in the sonic region

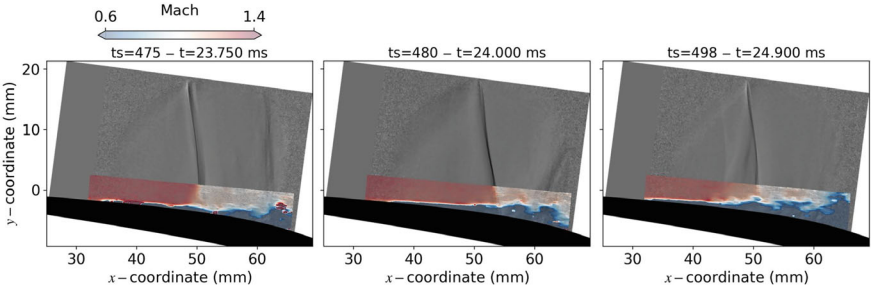

Fig. 9 Sequence of similar shock oscillation events from correlated HSS and HSPIV footage

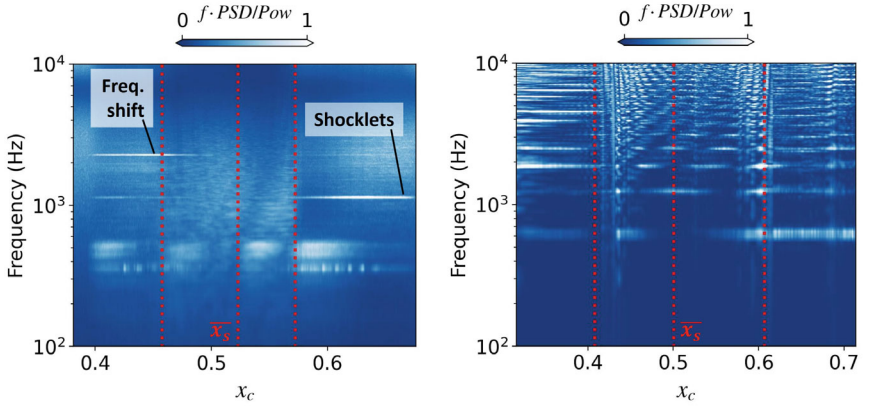

(a) Shadowgraphs' image intensity PSD (b) LES Density gradient magnitude PSD

Fig. 10 PSD contours comparison of the shock oscillation for experiments and LES results

of the flow. The different features shown in the figure and the sequence of the events then mirror very closely the ones identified from the LES results in Fig. 8.

One quantitative comparison is shown in this section with Fig. 7, which shows the PSD contours of the image gradient for the experiments and the density gradient magnitude for the LES. These contours were evaluated over a few pixel rows for the shadowgraphs and a similar interpolated probe line from the LES. The max., min. and mean positions of the shock are marked by red dotted lines in both contours. The contour from the experiments clearly shows that the region after the shock is dominated by the high-frequency tone at 1133 Hz. This frequency must then belong to the upstream movement of the shocklets, which occurs continuously throughout the cycle and at much higher rates than the movement of the main shock itself. The region affected by the shock is difficult to interpret given that it acts as a source and sink to the other features, although its main lower frequency band can still be identified. More interestingly, the region upstream of the shock shows a shift of energy towards the harmonic of the high-frequency tone at 2260 Hz.

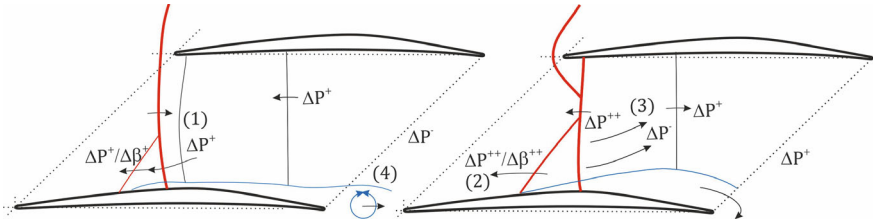

Fig. 11 Observed mechanisms of shock oscillation at the TCTA's ADP

Although the PSD of the LES results again shows itself to be much more tonal, it also shares a lot of the key traits previously noted. For instance, the high-frequency tones are again present downstream of the shock, and there is again a shift towards the higher tones of the most energetic frequencies. The region inside the shock is also difficult to interpret due to the appearance and disappearance of different frequency tones. However, wave propagation analyses via contours of the cross-correlation coefficient along the same pixel rows and probe lines reveal similar speeds of propagation of these shocklets. Further comparisons between both sets of data are shown and discussed in more detail in Munoz Lopez et al. [36]. These results demonstrate that the LES and the experiments are showing similar mechanisms of oscillation and prepares them for further analysis in the following section.

3.4 Mechanisms of SBLI Unsteadiness

By validating the LES results and leaning on the detailed data available of the whole flow field, the propagation of the pressure and flow incidence disturbances in the passage can be studied in detail. This analysis derived in the identification of at least two mechanisms of shock oscillation that are responsible for the different frequencies observed in the spectra from Fig. 7.

The mechanisms are summarized in Fig. 11. This schematic shows how the propagation of pressure waves in the subsonic region of the flow is continuous and occurs at high rates of propagation. When the shock is not inside the passage, the propagation of these waves continues in the sonic region in the form of weak oblique shocks (1). These shocks are only possible due to the easy propagation of these disturbances in the weak and uniform laminar boundary layer upstream of the shock. As the oblique shocks propagate upstream, they transmit the increase in pressure in the sonic region, but they also inevitably carry an increase in the flow angle upstream of the shock and therefore its position. This is how the movement of the shock is modulated by small oscillations at the high-frequency tones observed in the spectra, extending the mechanism of oscillation proposed in Hergt et al. [43].

When the propagation of the shocklets coincides with the main shock in the passage, strong interactions between these features lead to a strong pressure build-up that culminates in a stronger oblique shock propagating upstream (2). Just like before, as this oblique shock propagates, it inevitably carries both an increase in static pressure and the flow angle ahead of the shock. This oblique shock eventually reaches the leading edge of the adjacent upper blade and causes a strong oscillation of the operating point on the entire periodic domain. As the main shock moves upstream, the blocks of separated flow convecting downstream interact strongly with the flow in the passage (3). This generates regions of uneven flow properties that culminate in the pressure waves propagating upstream. The point at which these disturbances started propagating upstream is not unique, but was generally just upstream of the trailing edge in the region of 80% chord length.

In order to close the cycle, it was observed how the separated flow interacts strongly with the trailing edge of the profile, leading to a temporary vortex shedding from the trailing edge of the cascade (4). This vortex shedding seems to be responsible for the decreased static pressure at the outlet of the cascade that forces the shock to start moving back into the passage. Therefore, the manner and lag at which this interaction at the trailing edge occurs may be directly responsible for the actual main frequency of oscillation of the shock. Although the mechanisms described are inherently different from Lee's trailing edge feedback theory, this feature of the profile is still shown to have considerable significance in the way the whole cycle unfolds. For a lengthier discussion of the results and the mechanisms proposed, the reader is again referred to Munoz Lopez et al. [36].

4 Mitigating SBLI Unsteadiness with Flow Control Methods

In this last work package, the experience gathered from the previous sections is applied for the optimization of flow control methods (FCM) on the TCTA to mitigate its shock oscillations. For this purpose, a novel procedure has been developed to generate, mesh, and simulate the flow through any given blade with FCMs. This section then begins with a brief description of this optimization procedure developed, followed by the results obtained for a new TCTA configuration with roughness patches and reduced SBLI unsteadiness. For more details on the subject matter, the readers are referred to a later publication of the doctoral thesis by the authors.

4.1 A Novel Process Chain to Optimize Flow Control Methods

The design of compressor blades via numerical optimization typically requires an extensive amount of work and development before any shape can start being optimized. Most of this relates to the fully automated process chain necessary to parametrize, mesh, simulate, and evaluate any given optimization member. In this section, the process again employs the DLR's optimization suite, AutoOpti, along with the in-house CFD solver, TRACE. The latter was again used for (U)RANS simulations applying Menter's 2003 k-ω-SST model coupled with the 2009 version of his $\gamma - Re_{\Theta}$ transition model. For more details on these well-established packages, the reader is referred to the respective literature [23, 25, 44–46]. This section briefly presents the two main new software packages developed for the optimization of FCMs on compressor blades.

4.1.1 VortexGen: Parametrization and Generation of Blades with Flow Control Methods

The parametrization of the blade is performed with the in-house software BladeGen, which builds the blade with cubic B-spline surfaces defined by their control points and outputs the result in CAD files [23]. The surface is defined along the chord by the normalized u-coordinates, where values equal to 0, 1, 2, and 3 indicate the start of the pressure surface, leading edge, suction surface, and trailing edge, respectively. The normalized v-coordinate defines the hub and tip of the blade from 0 to 1. In order to add the FCMs, the newly developed software, VortexGen, receives the CAD output from BladeGen and applies the following routine for each FCM: a reference point is searched, the B-spline mesh in the region is refined, and the points within the region are modified based on the desired shape. With this framework, the FCMs shown in Fig. 12 and described below were implemented:

- **Roughness patch (RP)**: Defined by 5 design parameters, including a reference location (u, v), two lengths in spanwise and chordwise directions normalized by the chord (l_u, l_v), and the equivalent sand-grain roughness height (k_s).
- **Dome or dimple**: Defined by 5 parameters, including the reference location for the dome's center $(u, v)^{\text{center}}$, the maximum height (h), the radius from the center (r), and a stretch factor in the spanwise v-direction ($a_{uv} = r_v/r$). The height of the dome can be negative to create a dimple instead of a bump.
- **Ramp vortex generator (RVG) or plow**: Defined by a total of 9 design parameters. These include a reference location (u, v), a ramp angle (θ), its maximum height (h), total length and width (l, w), a width ratio parameter (p_w), and two lengths (l_{tip}, l_{edge}). The ratio p_w defines the angle of the ramp with respect to the chordwise direction.
- **Shock control bump (SCB) or plow**: Defined similarly as in Ogawa et al. [19] with a total of 12 parameters. These include a reference location (u, v); a length

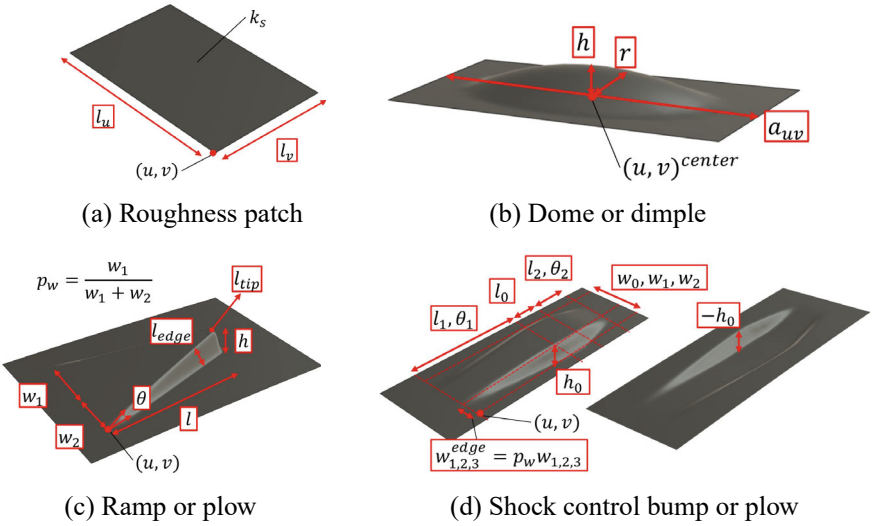

Fig. 12 Flow control methods parametrized and implemented in VortexGen for optimization procedures

and an angle for the front (l_1, θ_1) and rear (l_2, θ_2) ramps; a length and a height for the flat middle section (l_0, h_0); a total of three widths for each of these sections (w_0, w_1, w_2); and finally, a ratio parameter (p_w).

4.1.2 Centaur: Unstructured Meshing for Flow Control Methods

Just like the generation of the geometry itself, the meshing of a blade with FCMs can be an intricate procedure to automate. For this process chain, the unstructured mesher was used from the commercial software with scripting capabilities, Centaur. The domain is meshed with triangular prism layers for the blade's suction and pressure surfaces, two structured prism layer regions of hexahedral elements for the leading and trailing edges, and tetrahedral elements elsewhere. A number of refinement regions cover the bow shock area and the wake of the blade. A mesh convergence study was performed with the baseline TCTA configuration, from which appropriate mesh size and refinement factors were defined.

In order to automatically import and mesh any given TCTA configuration with FCMs, the python program, CentWrap, was developed. This program reads the output from VortexGen and creates an adapted set of scripts with refinement regions for the given FCMs and their wakes. The refinement sizes imposed are based on the most limiting features of the FCM, such as its height, width, rounding edge, or others depending on the FCM type. A series of mesh convergence studies were performed

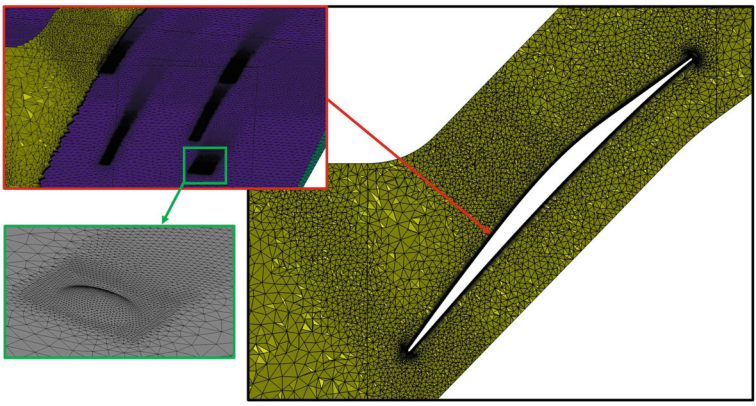

Fig. 13 Sample TCTA configuration with multiple flow control methods meshed automatically with Centaur and CentWrap

to ensure that the appropriate features and scaling factors were selected. A sample mesh of the TCTA with FCMs is shown in Fig. 13.

4.2 Optimization Strategy and Design Space

The remaining sections will focus on the optimization of a TCTA configuration with two RPs. The optimization of the remaining FCMs shown in Sect. 4.1.1 is left for the final publication of this doctoral work. In order to ensure that the SBLI effects were captured the best way possible within the scope of an optimization, a lot of effort was spent into testing and calibrating the numerical methods used. Afterward, a general optimization strategy was devised that could be adapted based on the type and number of FCMs to be optimized. This section presents an overview of said optimization strategy, along with a detailed rundown of the definition of the objective functions and the design space for the optimizations.

4.2.1 Simulating Unsteady SBLI Effects for Numerical Optimization

As shown in Sect. 3, capturing the unsteady effects from the SBLI in transonic cascade flows is not a trivial task. Recent experience comparing URANS with LES simulations revealed that excessively small timesteps ($\Delta t \approx 7.5$ ns) are required in URANS to capture similar oscillations [38]. This is a prohibitive timescale for the scope of the optimizations due to the long simulation times required to obtain converged statistics of the shock oscillation. The best option available was then to force the shock to oscillate with URANS simulations at more affordable timesteps

($\Delta t \approx 20\,\mu s$). With such timesteps, the simulation converges to the desired operating conditions, which are searched thanks to a new PID boundary conditions controller (BCC) developed. This controller can modify the input values at any boundary based on the rolling output of the simulation.

After the simulation converges to the desired operating conditions, the inflow angle at the inlet was modified by a delta based on a given input signal with zero average value. This signal was synthesized from a superposition of sine functions, where phase shifts are randomized and the amplitudes were taken from the spectrum of the shock oscillation in the experiments. This way, the shock inside the passage could be forced to oscillate with similar properties as in the experiments. These simulations were run for approximately 2000 timesteps, or about 20 cycles of the main target frequency from the experiments at nearly 500 Hz.

4.2.2 A Framework to Optimize Flow Control Methods

A general strategy was created to allow the optimization of different FCMs for the given objectives. This was achieved with a new Python program, OptiFCM, that is called by the optimizer and is able to set up and manage different optimization configurations. This program builds the process chain required for the imported configuration with the help of a number of custom classes that extend the functionalities offered by the job management software, FireWorks [47]. The latter allows the management of the process chain, so that if any issues arise or one of the constraints is not met, the process chain is defused. The results available are then returned to the optimizer to train the metamodel accordingly. The optimizations themselves follow a simple strategy, as visualized in Fig. 14 and described below:

1. A new member is provided by the optimizer to OptiFCM with a set of design parameters in order to create and launch the process chain.

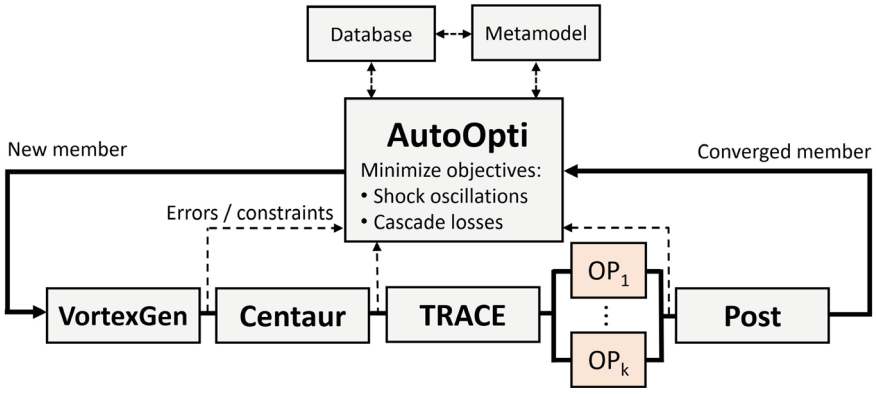

Fig. 14 Optimization strategy flowchart to mitigate SBLI unsteadiness with flow control methods

2. The VortexGen input files are created and the different geometrical constraints for the FCM types requested are calculated. The process chain is defused if one of the constraints is not met.
3. The output files from VortexGen are read by CentWrap and the scripts are generated to mesh the configuration with Centaur. The output files are checked to make sure the geometry was meshed without issues.
4. The output is compiled into a baseline TRACE simulation configuration, which is used to calculate each operating point requested. For the optimization results shown in this chapter, two operating points were simulated: the ADP, and an operating point near stall and at equal M_1 labeled as ODP1. However, the process chain supports any number of operating points desired. The simulations are checked for convergence and compliance to the constraints after every calculation.
5. The output of the converged URANS simulations is then post-processed to calculate the objective functions, which are discussed in the following sections.
6. Lastly, the results are passed to the optimizer, which updates the members database and the metamodel for the creation of the new members.

4.2.3 Optimization Objective Functions and Design Space

The goal of the optimization is to mitigate the unsteadiness of the shock in the passage, while maintaining or improving the performance of the cascade throughout its working range. In order to achieve this goal, the optimization was set to minimize two objective functions with the following formulations:

$$f_1 = \frac{\overline{\sigma}_{x_s}^{\mathrm{ADP}} + \overline{\sigma}_{x_s}^{\mathrm{ODP1}}}{2}, \qquad f_2 = \frac{\overline{\omega}^{\mathrm{ADP}} + \overline{\omega}^{\mathrm{ODP1}}}{2}, \tag{1}$$

where the first objective focuses on the standard deviation of the shock position signal captured inside the passage, σ_{x_s}. The standard deviations of the entire shock front tracked at each span (k) and pitch (j) locations of the 3D rectilinear probe grid sampled are averaged based on the variances of the signal as follows:

$$\overline{\sigma} = \sqrt{\frac{\sum^{n=j\times k} \sigma_{j,k}^2}{n}} \tag{2}$$

This same value is then averaged across the different operating points calculated. The objective f_2 on the other hand focuses on the total pressure loss coefficient of the cascade, as averaged over the course of the URANS with oscillating inlet conditions:

$$\overline{\omega} = \frac{\overline{P}_{01} - \overline{P}_{02}}{\overline{P}_{01} - \overline{P}_{1}} \tag{3}$$

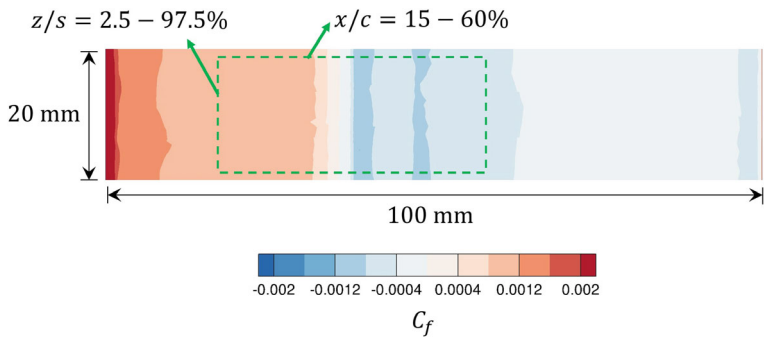

Fig. 15 Design space on the blade surface of the TCTA at the ADP for the optimization of flow control methods

The design space and constraints for the optimization are then defined for the two roughness patches to be optimized. The computational domain used for the simulations consists of periodic boundaries in the span and pitch directions of the cascade. The blade span was 20% of the blade chord, while the inlet and outlet boundaries are placed at one axial chord length upstream and downstream of the leading and trailing edges, respectively. The reference position is then freely set in u between 15 and 60% of the chord length, as shown in Fig. 15. The patches were centered in the v direction based on the value of its span length, l_v, which was freely set between 5 and 95%. The last free parameter, l_u, then determines the maximum u-position of each patch, $u_{\max}$. To ensure that the patches lie within the desired region and don't overlap, two constraints are added on $u_{\max}$ and the evaluated overlapping area between them. The de Haller number and mass flow are also constrained to have deltas no higher than ±2.5% with respect to the baseline to ensure that the operating conditions haven't changed considerably.

4.3 Results of an Optimized Roughness Patch Configuration

For this optimization, the design parameters for the RPs to optimize were set according to Fig. 15, with the length l_u limited to between 0.005–0.45, l_v and 0.025–0.950, and k_s to 0.0–70 (μm). With these settings, the configuration was optimized until a total of 310 members were calculated providing a well-populated Pareto front and satisfactory convergence criteria for the Kriging metamodel. The results will be presented in this section starting with the Pareto front itself, followed by a categorization of the best configurations obtained, and finally some of the perceived mechanisms of unsteady SBLI mitigation being applied.

4.3.1 Pareto Front Overview

The Pareto front obtained from the optimization is shown in green markers in Fig. 16. The members have been plotted by their fitness values in terms of the shock position standard deviation and the averaged cascade losses in the x- and y-axes, respectively. The "failed" members plotted are those that have reached the end of the process chain successfully, but have in the end failed the constraint on the averaged inlet Mach number. Most of these have highly unstable configurations and Mach numbers that are lower than the 1.19 limit set, and therefore show lower cascade losses than the rest. The reference member shown corresponds to the baseline configuration without any roughness patches applied on the suction surface.

Figure 16 quickly offers two main conclusions: the turbulent boundary layer is able to support and mitigate shock oscillations considerably, and the reduced severity of said oscillation can decrease the losses downstream of the cascade. That is, the unsteady flow generated from a severe oscillation of the shock naturally leads to higher losses from the increased turbulence and additional mixing that may occur in the wake. This despite the inevitable increase in viscous losses on the blade surface and the size of the boundary layer prior to the shock. Finally, depending on the intensity of the shock control action, the configuration can be tuned to equally optimal solutions from the Pareto front that either control the movement of the shock more strongly with higher losses or the other way around.

4.3.2 Categorizing the Best Members Calculated

The design parameters of the two RPs of the 16 Pareto front members with respect to the two fitness functions is shown in Fig. 17. From these graphs, it can be noted

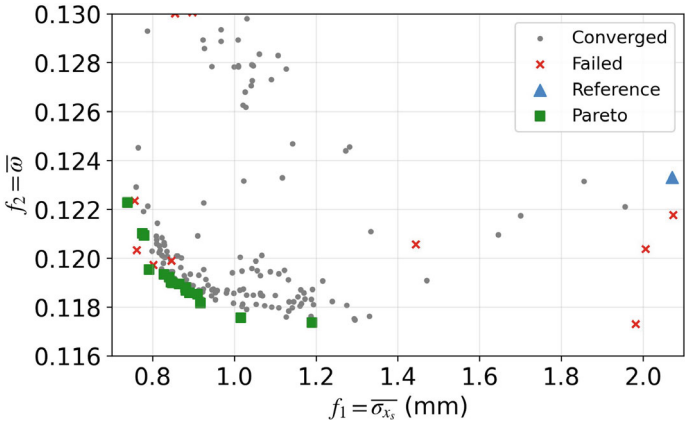

Fig. 16 Roughness patches optimization's Pareto front: avg. shock position standard deviation (x-axis) and avg. cascade losses (y-axis)

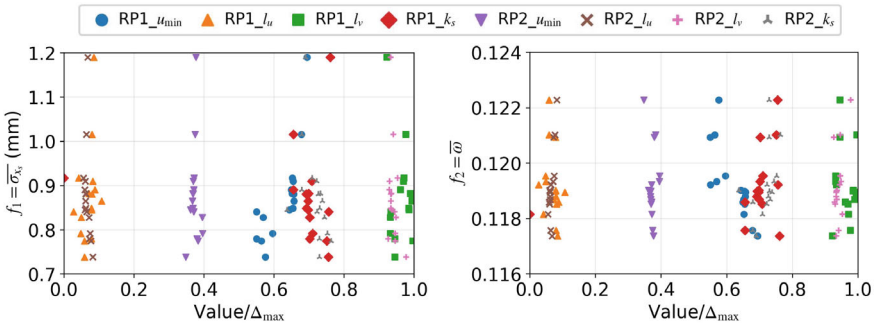

(a) Objective 1 (b) Objective 2

Fig. 17 Objective results of Pareto front members with respect to their scaled design parameters

Table 2 Optimization results for main members of the pareto front

	u_1	l_{u1}	l_{v1}	k_{s1} (μm)	u_2	l_{u2}	l_{v2}	k_{s2} (μm)	f_1 (mm)	f_2
Member 308	2.41	0.0311	0.900	52.9	2.30	0.0416	0.929	51.0	0.74	0.1223
Member 200	2.46	0.0428	0.879	53.3	2.32	0.0353	0.889	48.3	1.19	0.1174

that the optimizer converged to very similar values for most parameters. The main differences refer to the parameters of the first patch, RP1, placed further downstream than the second, RP2. Some configurations show that RP1 was not active, either with a k_s of nearly 0, or placed downstream of the shock ($\Delta u_1 > 0.65$), where it would have little effect on the separated flow. The figure also shows that a higher k_{s2} reduces the shock oscillation at the cost of higher losses. It can also be noted that the average non-scaled value of k_s and l_u for the RP2 of all members was 50.2 μm and 3.45 mm, respectively. Both shapes were also determined to be more effective when they extended over most of the blade span.

Two configurations are now looked at in more detail from the Pareto front: Member 308, with one of the lowest averaged standard deviations of the shock position and highest averaged losses, and Member 200, with the opposite characteristics. The design parameters and main optimization results for these two members are summarized in Table 2. The averaged solution of the URANS ADP simulation with oscillating inlet conditions is also shown for both members in Fig. 18. The figure shows the contours of the Mach number at the periodic boundary, as well as the friction coefficient over the blade surface. The areas where the roughness patch treatments were applied are also marked with black edges on the blade surface.

From both figures, it is clear that the most upstream roughness patch, RP2, trips the laminar boundary layer over the surface. In addition, the configuration with the stronger shock oscillations has RP1 placed far downstream of the shock. When RP1

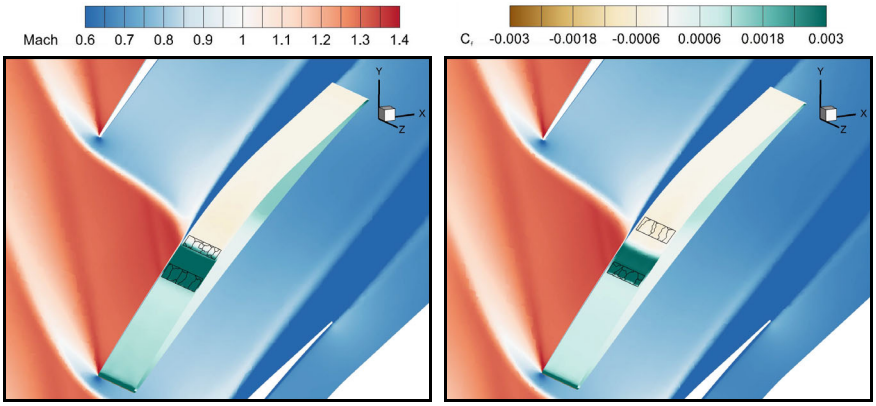

(a) Member 308 (b) Member 200

Fig. 18 Mach number and friction coefficient contours of averaged flow solutions of main Pareto front members at the ADP

is placed further upstream (Member 308), the oscillation of the shock is reduced by more than 64% when compared to the baseline configuration. The losses on the other hand have only marginally decreased by 0.8% of their original value. For Member 200 on the other hand, the oscillations of the shock are only reduced by 42%, but the averaged cascade losses have been reduced by 4.8% with respect to the baseline. Lastly, for both configurations, the ODP shows very similar contours (not shown), with the exception that the shock is further upstream and therefore the friction coefficient over the entirety of RP1 is negative. The shock position is still downstream of RP2, so that the incoming boundary layer is still turbulent.

4.3.3 On the Mitigation of Unsteady SBLI Effects

It has been determined that a well-placed RP can mitigate the oscillation of the shock and reduce the losses in the wake of the cascade. It can then be concluded that a turbulent boundary layer is able to withstand the oscillation of the shock better than a laminar one. To investigate this further, Fig. 19a is shown with the BL profiles just prior to the shock at 0.45 chord length from the URANS ADP simulations. In this figure, it can be observed that the laminar BL of the baseline configuration is already separated. This is due to the increased amplitude of oscillation of the shock, but also due to the earlier separation from the pressure gradient imposed by the shock. The BL for the two optimized members are shown to be more resilient, although they are difficult to compare with each other due to the different placement of the two RPs.

To take a closer look at the differences between the designs of both optimized members, their boundary layer profiles right at the beginning and end of RP2 are shown in Fig. 19b. In this graph, it is clear that how the boundary layer height, δ_{99},

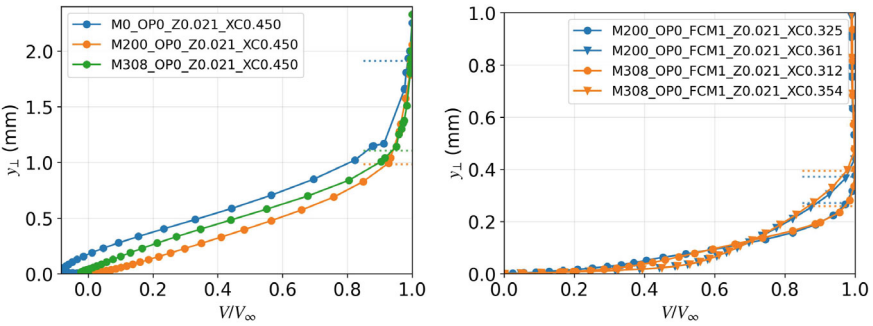

(a) At 45% blade chord (b) At start and end of roughness patch 2

Fig. 19 Boundary layer profiles comparison for the TCTA's baseline, Member 200, and Member 308 configurations

increases considerably over the length of the patch. However, the shorter and slightly lower roughness height of Member 200 seems to contribute to this member having a marginally smaller boundary layer and higher momentum near the BL edge. These slight differences may be playing a factor in the way and the location where the boundary layer separates near the shock. Therefore, it is not just the tripping of the boundary layer, but also the location and strength of the roughness applied to the flow that has contributed to the lower shock oscillations measured for this member.

5 Conclusions

In this chapter, the authors have given a brief overview of the comprehensive work package performed by the DLR for the TEAMAero consortium. This contribution aimed to improve the understanding of the unsteady SBLIs in transonic compressor cascades and propose novel methodologies to mitigate its effects. This was achieved by designing the Transonic Cascade TEAMAero, studying its cycle of shock oscillation, and finally by optimizing different configurations of flow control methods on its surface. The application throughout these work packages of both advanced numerical and experimental techniques allowed for detailed analysis of the results. This approach enhanced the conclusions obtained with respect to those that would have been possible if performed as isolated work packages.

The most relevant results to highlight showed that the oscillation of the shock on the TCTA is linked to mechanisms of interaction of the separated flow with the cascade's passage. Afterward, it was shown how a well-crafted optimization procedure can be developed to both mitigate the unsteady effects from these interactions and improve the performance of the cascade. These results exemplify the need to further integrate experimental and numerical methods in search of a deeper understanding of SBLI in transonic compressor cascades. Only the strong collaboration of numerous

stakeholders and disciplines will allow the consolidation of a global theory of SBLI in transonic compressor cascades.

Acknowledgements This work has received funding from the European Union's Horizon 2020 research and innovation program under grant agreement no. 860909. The LES simulations presented were performed on the national supercomputer HPE Apollo Hawk at the High Performance Computing Center Stuttgart (HLRS) under the grant number TCTA-SBLI/44238.
Competing Interests The authors have no conflicts of interest to declare that are relevant to the content of this chapter.

References

1. Ferri, A.: Investigations and experiments in the guidonia wind tunnel. Tech Memo NACA **901**, 1–33 (1939)
2. Fage, A., Sargent, R.F.: Shock-wave and boundary-layer phenomena near a flat surface. Math. Phys. Sci. (1947). https://doi.org/10.1098/rspa.1947.0058
3. Dussauge, J.P., Piponniau, S.: Shock/boundary-layer interactions: possible sources of unsteadiness. J. Fluids Struct. (2008). https://doi.org/10.1016/j.jfluidstructs.2008.06.003
4. Dolling, D.S.: Fifty years of shock-wave/boundary-layer interaction research: What next? AIAA J. (2001). https://doi.org/10.2514/2.1476
5. Lee, B.H.: Oscillatory shock motion caused by transonic shock boundary-layer interaction. AIAA J. (1990). https://doi.org/10.2514/3.25144
6. Pirozzoli, S., Grasso, F., Gatski, T.B.: DNS analysis of shock wave/turbulent boundary layer interaction at M = 2.25. In: 4th International Symposium on Turbulence and Shear Flow Phenomena (2005). https://doi.org/10.1615/tsfp4.2010
7. Dupont, P., Piponniau, S., Sidorenko, A., Debiève, J.F.: Investigation by particle image velocimetry measurements of oblique shock reflection with separation. AIAA J. (2008). https://doi.org/10.2514/1.30154
8. Crouch, J.D., Garbaruk, A., Magidov, D., Travin, A.: Origin of transonic buffet on aerofoils. J. Fluid Mech. (2009). https://doi.org/10.1017/S0022112009006673
9. Touber, E., Sandham, N.D.: Large-Eddy simulation of low-frequency unsteadiness in a turbulent shock-induced separation bubble. Theor. Comput. Fluid Dyn. (2009). https://doi.org/10.1007/s00162-009-0103-z
10. Epstein, A.H., Kerrebrock, J.L., Thompkins, W.T.: Shock structure in transonic compressor rotors. AIAA J. (1979). https://doi.org/10.2514/3.61134
11. Hergt, A., Klinner, J., Wellner, J., Willert, C., Grund, S., Steinert, W., Beversdorff, M.: The present challenge of transonic compressor blade design. J. Turbomach. (2019). https://doi.org/10.1115/1.4043329
12. Lee, B.H.: Self-sustained shock oscillations on airfoils at transonic speeds. Prog. Aerosp. (2001). https://doi.org/10.1016/S0376-0421(01)00003-3
13. Hartmann, A., Feldhusen, A., Schröder, W.: On the interaction of shock waves and sound waves in transonic buffet flow. Phys. Fluids (2013) https://doi.org/10.1063/1.4791603
14. Priebe, S., Wilkin, D., II, Breeze-Stringfellow, A., Mousavi, A., Bhaskaran, R., d'Aquila, L.: Large Eddy simulations of a transonic airfoil cascade. In: Proceedings of ASME Turbo Expo 2022 (2022). https://doi.org/10.1115/GT2022-80683
15. Ranjan Majhi, J., Venkatraman, K.: On the nature of transonic shock buffet in an axial-flow fan. AIAA J. (2023). https://doi.org/10.2514/1.j063318
16. Klinner, J., Hergt, A., Grund, S., Willert, C.E.: High-speed PIV of shock boundary layer interactions in the transonic buffet flow of a compressor cascade. Exp. Fluids (2021). https://doi.org/10.1007/s00348-021-03145-3

17. Pearcey, H.: Introduction to shock-induced separation and its prevention by design and boundary layer control. In: Boundary Layer and Flow Control (1961)
18. Mccullough, G., Nitzberg, G., Kelly, J.: Preliminary investigation of the delay of turbulent flow separation by means of wedge-shaped bodies. Res. Memo. NACA **A50L12**, 1–28 (1951)
19. Ogawa, H., Babinsky, H., Pätzold, M., Lutz, T.: Shock-wave/boundary-layer interaction control using three-dimensional bumps for transonic wings. AIAA J. (2008). https://doi.org/10.2514/1.32049
20. John, A., Qin, N., Shahpar, S.: Using shock control bumps to improve transonic fan/compressor blade performance. J. Turbomach. (2019). https://doi.org/10.1115/1.4042891
21. Klinner, J., Hergt, A., Grund, S., Willert, C.E.: Experimental investigation of shock-induced separation and flow control in a transonic compressor cascade. Exp. Fluids (2019)
22. Hergt, A., Klinner, J., Willert, C., Grund, S., Steinert, W.: Insights into the unsteady shock boundary layer interaction. In: Proceedings of ASME Turbo Expo 2022 (2022). https://doi.org/10.1115/GT2022-82720
23. Voß, C., Aulich, M., Kaplan, B., Nicke, E.: Automated multiobjective optimisation in axial compressor blade design. In: Proceedings of ASME Turbo Expo 2006 (2006). https://doi.org/10.1115/GT2006-90420
24. Aulich, M., Siller, U.: High-dimensional constrained multiobjective optimization of a fan stage. In: Proceedings of ASME Turbo Expo (2011). https://doi.org/10.1115/GT2011-45618
25. Schnoes, M., Voß, C., Nicke, E.: Design optimization of a multi-stage axial compressor using throughflow and a database of optimal airfoils. J. Glob. Power Propul. (2018). https://doi.org/10.22261/jgpps.w5n91i
26. Klose, B.F., Morsbach, C., Bergmann, M., Hergt, A., Klinner, J., Grund, S., Kügeler, E.: A numerical test rig for turbomachinery flows based on large Eddy simulations with a high-order discontinuous Galerkin scheme—Part II: Shock capturing and transonic flows. J. Turbomach. (2023). https://doi.org/10.1115/1.4063827
27. Morsbach, C., Bergmann, M., Tosun, A., Klose, B.F., Bechlars, P., Kügeler, E.: A numerical test rig for turbomachinery flows based on large Eddy simulations with a high-order discontinuous Galerkin scheme—Part 3: Secondary flow effects. In: Proceedings of ASME Turbo Expo 2023 (2023). https://doi.org/10.1115/GT2023-101374
28. Bergmann, M., Morsbach, C., Klose, B.F., Ashcroft, G., Kügeler, E.: A numerical test rig for turbomachinery flows based on large Eddy simulations with a high-order discontinuous Galerkin scheme—Part I: Sliding interfaces and unsteady row interactions. J. Turbomach. (2023). https://doi.org/10.1115/1.4063734
29. Munoz Lopez, E.J., Hergt, A., Grund, S.: The new chapter of transonic compressor cascade design at the DLR. In: Proceedings of ASME Turbo Expo 2022 (2022). https://doi.org/10.1115/GT2022-80189
30. Munoz Lopez, E.J., Hergt, A., Grund, S., Gümmer, V.: The new chapter of transonic compressor cascade design at the DLR. J. Turbomach. (2023). https://doi.org/10.1115/1.4056982
31. Menter, F.R., Kuntz, M., Langtry, R.: Ten years of industrial experience with the SST turbulence model turbulence heat and mass transfer. Turbul. Heat Mass Transf. **4**(625–632), 2003 (2023)
32. Langtry, R.B., Menter, F.R.: Correlation-based transition modeling for unstructured parallelized computational fluid dynamics codes. AIAA J. (2009). https://doi.org/10.2514/1.42362
33. Starken, H., Schimming, P., Breugelmans, F.A.: Investigation of the axial velocity density ratio in a high turning cascade. In: Proceedings of ASME Turbo Expo 1975 (1975). https://doi.org/10.1115/75-GT-25
34. Munoz Lopez, E.J., Hergt, A., Ockenfels, T., Grund, S., Gümmer, V.: The current gap between design optimization and experiments for transonic compressor blades. Int. J. Turbomach. Propul. Power (2023). https://doi.org/10.3390/ijtpp8040047
35. Schodl, R.: Laser dual-beam method for flow measurements in turbomachines. In: Proceedings of ASME Turbo Expo 1974 (1974). https://doi.org/10.1115/74-GT-157
36. Munoz Lopez, E.J., Hergt, A., Klinner, J., Klose, B., Willert, C., Guemmer, V.: The unsteady shock-boundary layer interaction in a compressor cascade—Part 3: Mechanisms of shock oscillation. In: Proceedings of ASME Turbo Expo 2024 (2024)

37. Klinner, J., Munoz Lopez, E.J., Hergt, A., Willert, C.: The unsteady shock-boundary layer interaction in a compressor cascade—Part 1: Measurements with time-resolved PIV. In: Proceedings of ASME Turbo Expo 2024 (2024)
38. Klose, B.F., Morsbach, C., Bergmann, M., Munoz Lopez, E.J., Hergt, A., Kügeler, E.: The unsteady shock-boundary layer interaction in a compressor cascade—Part 2: High-fidelity simulation. In: Proceedings of ASME Turbo Expo 2024 (2024)
39. Klinner, J., Munoz Lopez, E.J., Hergt, A., Willert, C.: High-resolution PIV measurements of the shock boundary layer interaction within a highly loaded transonic compressor cascade. In: 15th International Symposium on Particle Image Velocimetry (2023). Available via eLib. https://elib.dlr.de/197278/. Cited 11 June 2024
40. Munoz Lopez, E.J., Hergt, A., Klinner, J., Grund, S., Flamm, J., Gümmer, V.: Investigations of the unsteady shock-boundary layer interaction in a transonic compressor cascade. In: Proceedings of ASME Turbo Expo 2023 (2023). https://doi.org/10.1115/GT2023-102622
41. Schlüß, D., Frey, C., Ashcroft, G.: Consistent non-reflecting boundary conditions for both steady and unsteady flow simulations in turbomachinery applications. In: ECCOMAS Congress 2016—Proceedings 7th European Congress on Computational Methods in Applied Sciences and Engineering (2016). https://doi.org/10.7712/100016.2342.5411
42. Pirozzoli, S.: Numerical methods for high-speed flows. Ann. Rev. Fluid Mech. (2011). https://doi.org/10.1146/annurev-fluid-122109-160718
43. Hergt, A., Klose, B., Klinner, J., Bergmann, M., Munoz Lopez, E.J., Grund, S., Morsbach, C.: On the shock boundary layer interaction in transonic compressor blading. In: Proceedings of ASME Turbo Expo 2023 (2023). https://doi.org/10.1115/GT2023-103218
44. Siller, U., Voß, C., Nicke, E.: Automated multidisciplinary optimization of a transonic axial compressor. In: 47th AIAA Aerospace Sciences Meeting (2009). https://doi.org/10.2514/6.2009-863
45. Becker, K., Heitkamp, K., Kuegeler, E.: Recent progress in a hybrid-grid CFD solver for turbomachinery flows. In: Procedings of 5th European Conference on Computational Fluid Dynamics ECCOMAS (2010)
46. Ashcroft, G., Heitkamp, K., Kügeler, E.: High-order accurate implicit Runge-Kutta schemes for the simulation of unsteady flow phenomena in turbomachinery. In: Proceedings of 5th European Conference on Computational Fluid Dynamics ECCOMAS (2010)
47. Jain, A., Ong, S.P., Chen, W., Medasani, B., Qu, X., Kocher, M., Brafman, M., Petretto, G., Rignanese, G.M., Hautier, G., Gunter, D., Persson, K.A.: Fireworks: a dynamic workflow system designed for high throughput applications. Concurr. Comp.-Pract. E (2015). https://doi.org/10.1002/cpe.3505